Adjustable topological corner states in terahertz valley photonic crystals

Gong-Hui Tang,[1] Yu-Liang Hong,[1] Rui-Li Zhang,[1,*] Ren-Hao Fan,[1,†] Zhong-Li Ma,[1] Xiang-Yu Wu,[1] Dong-Xiang Qi,[1] Ru-Wen Peng,[1,‡] and Mu Wang[1,2,§]

[1]*National Laboratory of Solid State Microstructures, School of Physics, and Collaborative Innovation Center of Advanced Microstructures, Nanjing University, Nanjing 210093, China*
[2]*American Physical Society, Hauppauge, New York 11788, USA*

(Received 14 June 2023; revised 11 October 2023; accepted 16 October 2023; published 9 November 2023)

Higher-order topological insulators (HOTIs) have emerged as unique topological materials hosting topological corner or hinge states. This work investigates terahertz (THz) higher-order topological states in C_3 symmetric valley photonic crystals (VPCs) in theory and experiment. Based on numerical simulations of photonic band structure, phase profiles, and Berry curvature, we realize the valley topological phase transition by rotating the scatterers in unit cells. Meanwhile, the higher-order topology of the VPCs is characterized by nontrivial bulk polarization. The topological corner states are demonstrated by calculated eigenenergy spectra, field distributions, and local density of states of nested triangular structures. In addition, the associated fractional corner charge is also employed to confirm the existence of topological corner states directly. Two topological corner states are identified, one staying within band gap and the other embedding in bulk bands. Both originate from quantized bulk dipole moments and are flexibly switchable by rotating the scatterers of the system. Experimentally angle-resolved transmittance measurements demonstrate the presence of the photonic band structure and the bulk band gap of the THz photonic crystals. The measured time-domain spectra reveal the valley edge states between distinct THz VPCs. Further, we directly observe the topological corner states in the measured spatial mapping of the electric field intensity. These investigations testify to the possibility of simultaneously employing topological corner, edge, and bulk states to guide THz waves, which may have potential applications in THz functional devices.

DOI: 10.1103/PhysRevB.108.205411

I. INTRODUCTION

The topological system has expanded from condensed-matter physics to photonic [1,2], phononic [3–5], and other classical systems [6,7] in the past decade. A unique class of topological materials known as higher-order topological insulators (HOTIs) has recently been introduced. In contrast to conventional topological insulators, where the topological edge states have one dimension lower than the bulk states, HOTIs have boundary states two or more dimensions lower than the bulk states, such as corner or hinge states [8–11]. In the early studies, zero-dimensional (0D) topological corner states, characterized by the quantized bulk multipole moments, arise from edge-localized dipole moments observed in quantized multipole insulators of finite samples [8,9,12–16]. Later, inspired by 0D topological edge states in the one-dimensional (1D) Su-Schrieffer-Heeger model, topological corner states can be constructed in the generalized higher-dimensional models, which have the characteristics of quantized bulk dipole moments [8–10,17–24]. In addition, some topological defects in the real space of topological crystalline insulators can also be regarded as topological corner states [9,25,26]. Despite being generated in various ways, topological corner states exhibit fractional charge at corners, which is one of the critical features of higher-order topology. Hence, the fractional corner charge has also been employed to identify topological corner states directly [26–28]. Topological corner states offer a novel approach towards robustly confining light, which may enable potential applications such as cavity modes with a high-quality factor [29], crystal fibers [30], and low-threshold topological lasing [31,32]. So far, HOTIs with corner states have been demonstrated in various structures such as two-dimensional (2D) square lattices [12–21], Kagome lattices [22–24], and so on. Lately, it has also been realized in the valley system [33–36].

Valley degree of freedom was first proposed in 2D hexagonal crystals, which refers to a pair of degenerated but inequivalent states of energy extrema in the momentum space [37,38]. The materials with valley degrees of freedom exhibit a local nontrivial valley Hall effect when inversion or mirror symmetry is broken [39–41]. Generally, the valley-polarized topological edge states emerge at the domain walls of topologically distinct regions [39–41] and connect lower and upper bulk bands. It is possible to open a large band gap and even enter a fully gapped regime for the structure with zigzag edge domain walls [42]. In recent years, with the introduction of HOTIs, it has been demonstrated that higher-order valley-selective topological corner states can exist in the band gap of

*rlzhang@nju.edu.cn
†rhfan@nju.edu.cn
‡rwpeng@nju.edu.cn
§muwang@nju.edu.cn

C_3 symmetric valley photonic crystals (VPCs) [33–36], which is characterized by the nontrivial bulk polarization. Because of localization within the band gap, these corner states can be identified and characterized easily. C_3 symmetry in the system protects the degeneracy of valley-selective topological corner states but does not restrict their energy [26]. Therefore, it implies that topological corner states can appear within the band gap and be embedded in the bulk band, depending on the band structure.

On the other hand, topological photonics also brings new vitality to develop unique functional materials and devices, including terahertz (THz) ones. Terahertz is considered as a promising frequency regime due to its large bandwidth [43,44] and high security [45]. Up to now, based on robust topological edge states, people have successfully realized potential THz devices, such as THz low-loss waveguides [41,46], on-chip demultiplexers [47], and THz quantum cascade lasers [48]. The efforts introducing higher-order topology to THz photonics [36,49,50] have been implemented in theory, and corner states are obtained which provide a new degree of freedom for manipulating THz waves. However, the investigations have focused on the topological corner states within the band gap.

In this work we theoretically and experimentally demonstrate valley topological transition and the generation of higher-order corner states in THz photonic crystals. Firstly, the designed VPCs are characterized by calculated photonic band structure, phase profiles, and Berry curvature. Then we construct nested triangular structures and verify the presence of topological corner states by calculating eigenenergy spectra, field distributions, and local density of states (LDOS). In addition, the corner charges have been evaluated. When the corner charges are integers, there is no topological corner state. However, when the corner charges are fractional, it indicates the existence of topological corner states. Interestingly, there are two types of topological corner states: one is lying in the band gap, which is usual and similar to previous reports [33–36]. The other appears within bulk bands because symmetry reduction is insufficient to open a wider band gap, forming embedded corner states in bulk bands. Simply by rotating the scatterers of the system, the band gap can be tuned, and the two types of corner states can be switched between each other flexibly. In the experiments we fabricate a series of THz VPC samples. By measurements, the valley topological edge states and the two types of corner states are experimentally observed. The investigations bring possibilities for simultaneously employing topological corner, edge, and bulk states to guide THz waves.

This paper is arranged as follows. After the Introduction, we present the valley topological phase transition and higher-order topology of the designed THz VPCs in Sec. II. In Sec. III we elaborate on forming two topological corner states by constructing nested triangular structures. Also, we illustrate the absence of corner states in some cases. Then the fractional corner charge is obtained to identify the topological corner states. In Sec. IV the THz experiments are implemented to confirm the existence of both topological valley edge states and the two types of topological corner states in the system. The results are summarized in Sec. V.

II. HIGHER-ORDER TOPOLOGICAL PHASES IN C_3 SYMMETRIC VALLEY PHOTONIC CRYSTALS

The designed 2D photonic crystal is arrayed in a triangular lattice, where the hexagonal unit cell is composed of three identical metal cylinders embedded in air, as shown in the left panel of Fig. 1(a). The lattice vectors are $\boldsymbol{a_1} = (a, 0)$ and $\boldsymbol{a_2} = (a/2, a\sqrt{3}/2)$, with the lattice constant $a = 475\ \mu\text{m}$. We set the diameter of the metal cylinders as $d = 200\ \mu\text{m}$, and every three cylinders are tangent together to form a cloverlike trimer. In the unit cell, the rotation angle θ is defined as the angle between one of the principal axes of the trimer and the x axis, with counterclockwise rotation as the positive direction, as shown in the right-top panel of Fig. 1(a). The bottom-right part of Fig. 1(a) shows the first Brillouin zone (FBZ) of the triangular lattice. In the case of $\theta = 0^\circ$, the 2D photonic crystal possesses a pair of degenerate Dirac points at K and K′ valleys at 0.29 THz due to the C_{3v} symmetry, and the photonic band structure is shown in Fig. 1(b). The calculations on the photonic band structures of THz photonic crystals have been carried out using a commercial software package (COMSOL MULTIPHYSICS), and periodic boundary conditions have been applied to the system. Here only the transverse electric mode is considered. The metal cylinders of the photonic crystals have been assumed to be perfect electric conductors within the targeted THz frequency range. We introduce a geometrical perturbation by rotating the trimer with an arbitrary angle in the unit cell. In this process the original C_{3v} symmetry is reduced to the C_3 symmetry. It results in the lifting of degeneracy at the K (and K′) valley and the opening of a band gap. Without losing generality, we choose the photonic crystals with $\theta = 15^\circ$ and $\theta = -15^\circ$, and calculate their band structures and phase profiles. As shown in Fig. 1(c), despite their identical band structure due to mirror symmetry, the corresponding frequencies of the left circularly polarized (LCP) and right circularly polarized (RCP) light are reversed at the K valley [as shown in the middle of Fig. 1(c)], indicating a typical topological phase transition.

The topological phase transition is related to the rotating angle θ. As illustrated in the topological phase diagram of the VPC in Fig. 2(a), the exchange of states with opposite chirality occurs at $\theta = 0^\circ$ or $\theta = \pm 60^\circ$, where the mirror symmetry resumes. Such a transition can occur with a periodicity of 120° for the phase diagram due to the C_3 symmetry of the VPC. To better understand the topological phase transition, we have calculated the distribution of Berry curvature of the first band in the FBZ. Here we choose the VPCs with $\theta = 30^\circ$ (VPC30_+) and $\theta = -30^\circ$ (VPC30_-). As shown in Fig. 2(b), the Berry curvature is opposite in sign for the K and K′ valley for a certain VPC. In addition, the Berry curvature is reversed at the same valley in the case of the opposite sign of the rotation angle θ. By integrating the Berry curvatures around K or K′ valley, the valley Chern numbers have been achieved, which are $C_K = -1/2$ and $C_{K'} = 1/2$ when $\theta > 0^\circ$, and $C_K = 1/2$ and $C_{K'} = -1/2$ when $\theta < 0^\circ$, respectively.

The bulk polarization of our VPCs has been evaluated to reveal the nontrivial higher-order topology. In a 2D system, the bulk polarization [9,10] is defined in terms of the Berry

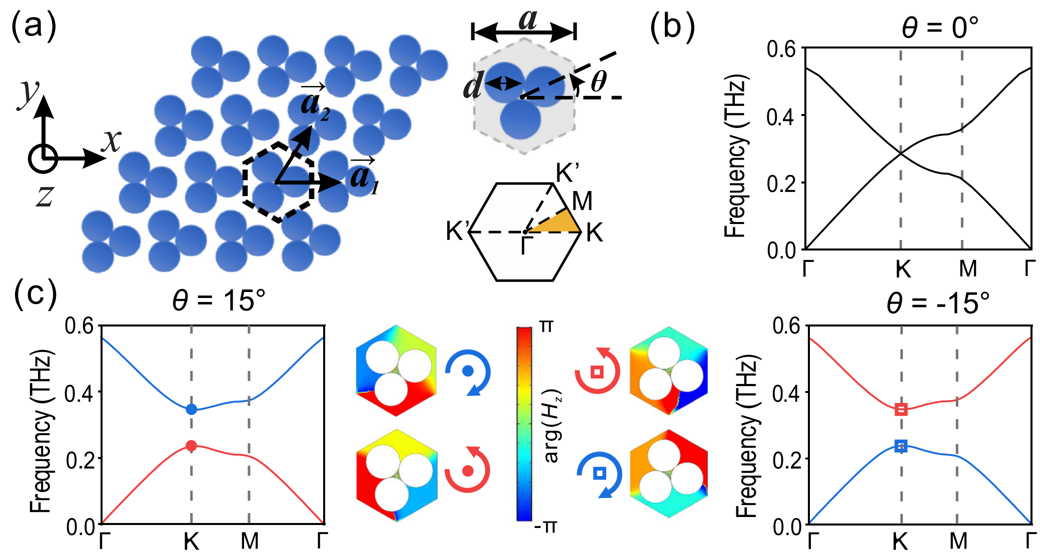

FIG. 1. (a) Schematic of the photonic crystal. The diameter of cylinder d is 200 μm, and the lattice constant a is 475 μm. The rotation angle θ of the cylinder location is the angle between one of principal axes of the unit cell and the x axis. The unit cell and the FBZ are shown on the right. (b), (c) Band structures of the photonic crystals with (b) $\theta = 0^\circ$, (c) $\theta = 15^\circ$ and $\theta = -15^\circ$, respectively. The phase profiles of H_z at the K valley for cases of $\theta = 15^\circ$ and $\theta = -15^\circ$ are shown in the middle, and the blue and red arrows denote LCP and RCP states, respectively.

connection as

$$P_\tau = -\frac{1}{(2\pi)^2}\int_{FBZ} d^2k Tr[A_\tau], \tag{1}$$

where τ indicating the component of P along the reciprocal lattice vector b_τ $(\tau = 1, 2)$, and $[A_\tau(k)]^{mn} = -i\langle u^m(k)|\partial k_\tau|u^n(k)\rangle$ is the Berry connection matrix where m and n run over occupied energy bands, and $|u^n(k)\rangle$ is the periodic Bloch function for the nth band with the wave vector k. The Wilson loop approach can achieve the two components of bulk polarization [9,51],

$$P_\tau = -\frac{1}{2\pi}\int_L d\nu_{\tau,b_\eta}. \tag{2}$$

Here L denotes the projection length of the FBZ along the b_η direction. ν_{τ,b_η} is the Berry phase along the loop b_τ for a fixed b_η. The gray region of Fig. 2(c) shows the FBZ in the calculations, which is adapted by deforming the hexagon to a rhombus. To show the polarization evolution in our VPCs, we have calculated P_1 under the case of different θ plotted in Fig. 2(d). In the regime of $\theta \in (-60^\circ, 60^\circ)$, there are two kinds of nonzero bulk polarization corresponding to two distinct higher-order topological phases. For $\theta \in (-60^\circ, 0^\circ)$, P_1 is approximately equal to 1/3; while for $\theta \in (0^\circ, 60^\circ)$, P_1 is about equal to –1/3. Since the two reciprocal vectors, $\boldsymbol{b_1}$ and $\boldsymbol{b_2}$, are related by the C_3 symmetry in the FBZ, we can get $P_2 = P_1$. Therefore the bulk polarization $\boldsymbol{P}$ of our VPC along $\boldsymbol{b}_{1,2}$ can be obtained: $\boldsymbol{P} = (1/3, 1/3)$ $(-60^\circ < \theta < 0^\circ)$ and $\boldsymbol{P} = (-1/3, -1/3)$ $(0^\circ < \theta < 60^\circ)$, and higher-order topological phase transition occurs at $m\pi/3$ $(m = \cdots -1, 0, 1 \cdots)$.

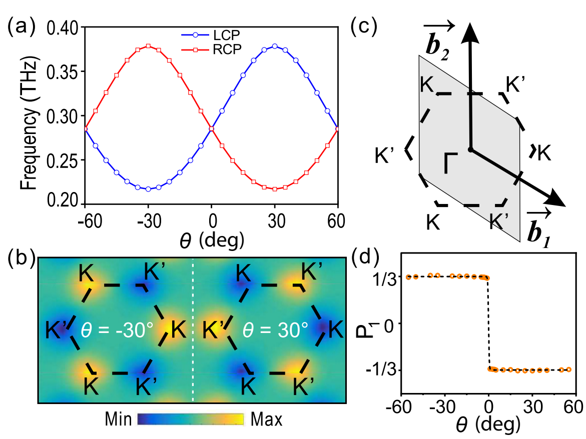

FIG. 2. (a) Calculated eigenfrequencies of LCP (blue curve) and RCP (red curve) states at the K valley when θ varies. (b) Distribution of Berry curvature when $\theta = -30^\circ$ (left panel) and $\theta = 30^\circ$ (right panel). (c) The rhombic BZ (gray region) in the numerical calculations of bulk polarization components is deformed from the original hexagonal BZ (dashed line region). (d) Calculated polarization component P_1 as a function of θ using Wilson loop methods, orange circles represent simulations.

III. GENERATION OF TWO TYPES OF TOPOLOGICAL CORNER STATES

To demonstrate the existence of higher-order corner states, we construct nested triangular structures made of VPCs with distinct topological phases. First, type-A structures are built when the VPC with $\theta > 0^\circ$ is surrounded by the VPC with $\theta < 0^\circ$. Specifically, the VPC30$_+$ is surrounded by the VPC30$_-$ to form a type-A30 structure in Fig. 3(a), and the VPC15$_+$ is surrounded by the VPC15$_-$ to create a type-A15 structure as shown in Fig. 3(d). It is observed that edge and corner states exist in the bulk band gap of type-A30 structure from the eigenenergy spectra presented in Fig. 3(b). In particular, three degenerate corner states appear in the band gap between the edge and bulk states. It can also be demonstrated

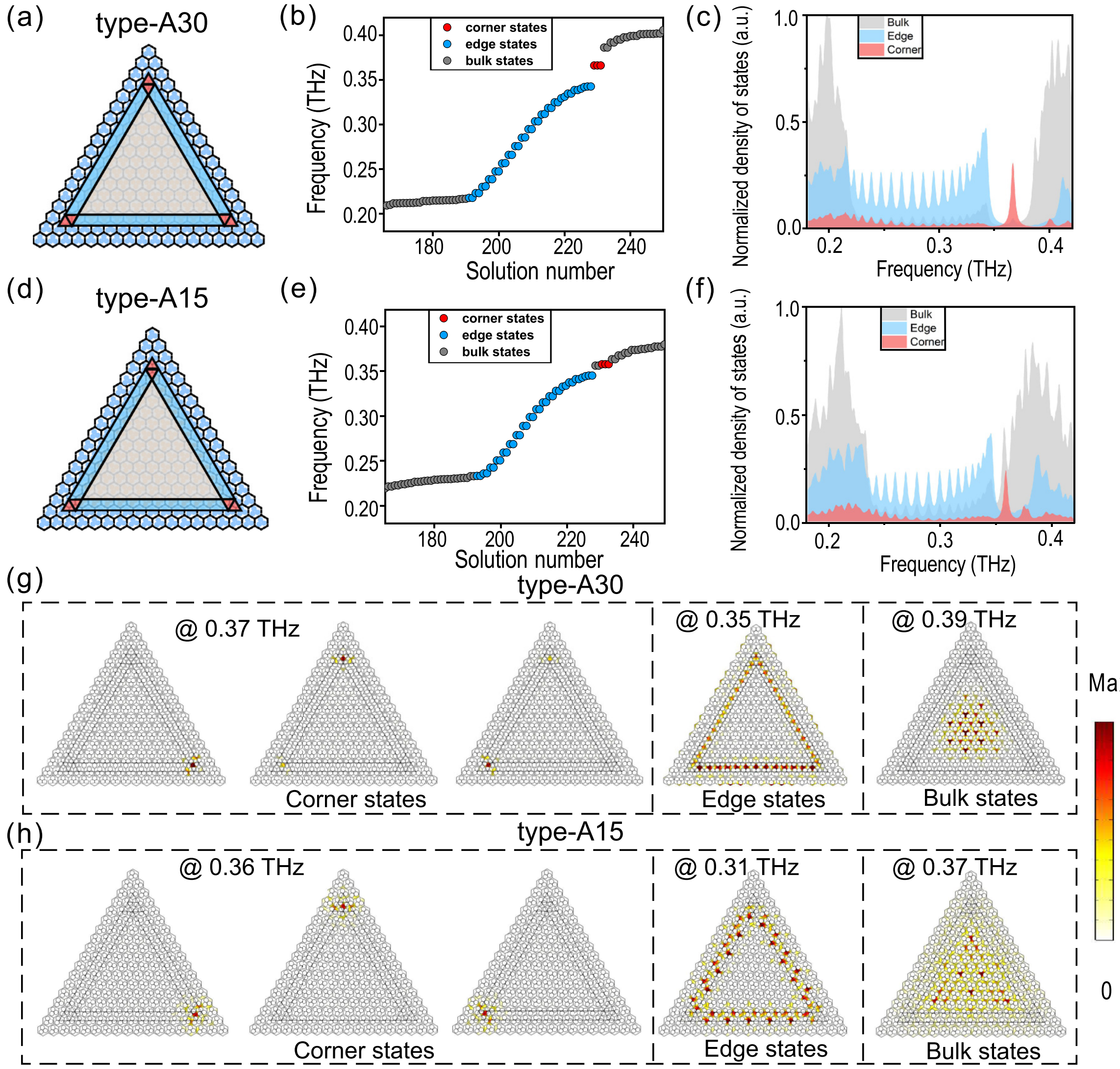

FIG. 3. Schematic of (a) type-A30 and (d) type-A15 nested triangular structures. Gray, blue, and red shadows represent bulk, edge, and corner regions, respectively. (b) and (e) Numerically calculated eigenenergy spectra corresponding to (a) and (d), respectively. (c) Type-A30 and (f) type-A15 show calculated LDOS spectra. Here, a.u. stands for arbitrary units. The intensity distributions of $|H_z|$ for corner, edge, and bulk states are displayed in (g) type-A30 and (h) type-A15. In the calculations, the inner part of the nested triangular structure is 12 unit cells long and is surrounded by two layers of the outer part. Perfect electric conductor boundary conditions have been used.

from the distributions of the magnetic field in Fig. 3(g), where the corner states at 0.37 THz are well localized around the corners, and the edge state at 0.35 THz and bulk state at 0.39 THz are displayed clearly in type-A30 structure. Interestingly, for the type-A15 structure, three corner states also appear but are embedded in the continuum of the bulk states [as shown in Fig. 3(e)]. It is because the band structure can be deformed simultaneously, in which the band gap is closed and reopened, by rotating the anisotropic scatterers continuously. With the rotation angle of 15°, symmetry reduction of the system is insufficient to open a bulk band gap wide enough. Nevertheless, corner states are hardly affected by the deformation of bulk bands, suggesting the topologically protected property. As a result, such corner states are embedded in bulk bands, i.e., for type-A15 structure, corner states and bulk states are overlapped in frequency but are fully localized to the corner. By calculating the distributions of the magnetic field, it is found that the corner states are distinguishable [shown in Fig. 3(h)]. Specifically, the magnetic fields of corner states at 0.36 THz are confined around the corners with almost no leakage into the bulk or edge region, but they become “leaky” when the required symmetries are broken. For comparison, the edge and bulk states are also demonstrated in Fig. 3(h) for the type-A15 structure. Furthermore, the LDOS for the corner, edge, and bulk regions [illustrated in Figs. 3(a) and 3(d)] can be used to reveal the spectral features of corner states. The photonic LDOS $\rho(r,\omega)$ is calculated by [26,27]

$$\rho(r,\omega)=\sum_n \frac{\Gamma}{\pi}\frac{\left|H_z^{(n)}(r)\right|^2}{(\omega-\omega_n)^2+\Gamma^2}, \tag{3}$$

where n indicates the order number of photonic eigenstates, and $\Gamma\rightarrow 0$ is a sufficiently small number that converges the calculation. $H_z^{(n)}(r)$ is the scaled magnetic field distribution

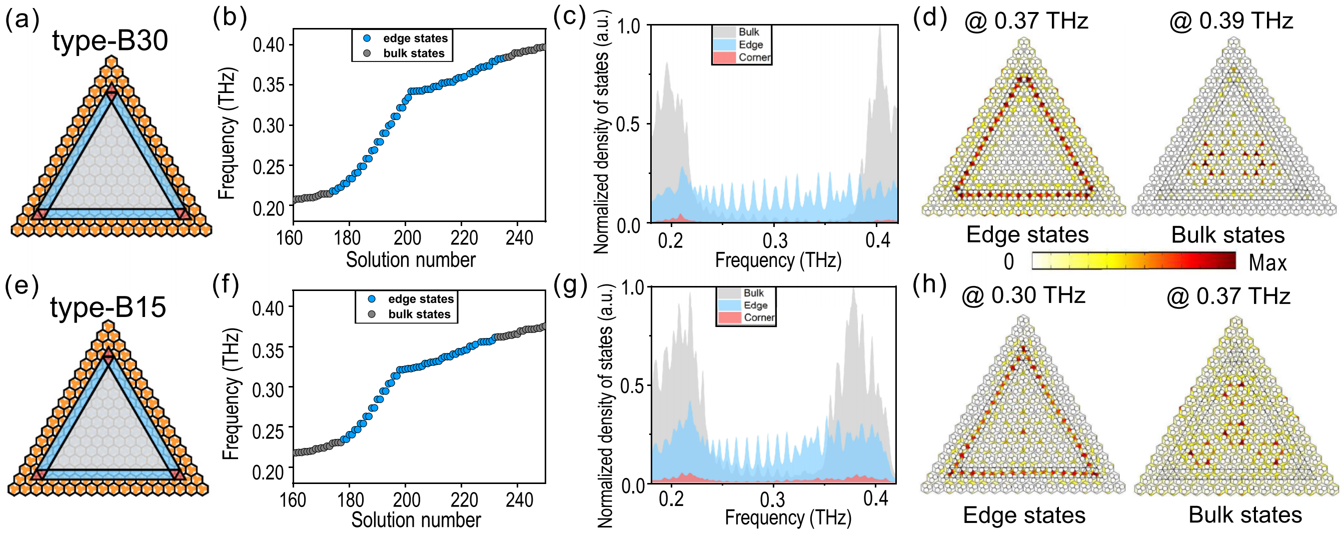

FIG. 4. Schematic of (a) type-B30 and (e) type-B15 nested triangular structure. Gray, blue, and red shadows represent bulk, edge, and corner regions, respectively. (b) and (f) Calculated eigenenergy spectra corresponding to (a) and (e), respectively. (c) Type-B30 and (g) type-B15 show numerically calculated LDOS spectra. The intensity distributions of $|H_z|$ for corner, edge, and bulk states in (d) type-B30 and (h) type-B15.

of the nth photonic eigenstate that satisfies the normalization condition of

$$\int dr\left|H_z^{(n)}(r)\right|^2 = 1, \tag{4}$$

where the integral of r is over the whole photonic system. It is found from the LDOS spectra depicted in Fig. 3(c) that type-A30 structure exhibits conventional distinguishable features of corner states: the emergence of a sharp peak of corner states around 0.37 THz within the bulk band gap. Remarkably, for the type-A15 structure, the corner states also emerge as a sharp peak at around 0.36 THz, overlapping with the spectra of the bulk states [shown in Fig. 3(f)]. Discrete corner states can be generated in the type-A15 structure even though their spectral peaks may overlap with the bulk continuum. If we deliberately rotate the scatterers of the unit cells in the type-A structures, topological corner states can appear in the band gap or the bulk continuum controllably. Therefore two types of topological corner states are obtained: one is lying within the band gap, and the other is embedded within bulk bands. They are flexibly switchable by rotating the scatterers of type-A structures.

In addition, type-B nested triangular structures are constructed when the VPC with $\theta < 0^\circ$ is surrounded by the VPC with $\theta > 0^\circ$, as shown in Figs. 4(a) and 4(e). Differently, the eigenenergy spectra show bulk and edge states, while there is no sign of corner states either in type-B30 or type-B15 structure [Figs. 4(b) and 4(f)]. This feature is further corroborated by the calculated LDOS spectra [Figs. 4(c) and 4(g)] and magnetic field distributions [Figs. 4(d) and 4(h)]. Consequently, the type-B structures have bulk and edge states without corner states.

It should be noted that corner states either in the band gap or within bulk bands originate from quantized bulk polarization. The quantized bulk polarization is protected by the C_3 symmetry of type-A structures, but the C_3 symmetry does not constrain the energy of corner states, so corner states can appear in the band gap or bulk bands of eigenenergy spectra. However, the eigenenergy spectra of type-B structures with quantized bulk polarization do not exhibit the characteristic of corner states. This is because the emergence of corner states also depends on corner shape, which is generally related to the separation of Wannier centers. Wannier centers are the expected value of the electronic positions relative to the center of positive charge within the unit cell [9,10], associated with the bulk polarization. And nonzero bulk polarization suggests that the Wannier centers may appear at the boundary of the unit cell. Therefore the separation of Wannier centers can lead to the generation of fractional charges at the boundary. When the Wannier center overlaps with the geometric corner site, topological corner states with fractional charge will be generated for the finite samples. This is essential to distinguish topologically protected corner states from other local modes. In Fig. 5(a) we have depicted the schematic of a type-A structure with hidden outer layers. The geometric corner sites overlap with Wannier centers, which induces the separation of Wannier centers and leads to a fractional charge at the corners. Moreover, due to the C_3 symmetry of the system, the corner charge is predicted to be fractional to 1/3 or 2/3 (mod 1). However, the Wannier center configuration in Fig. 5(b) indicates no fractional charge for the type-B structure.

To confirm the above analysis, we evaluate the photonic "charge" of the system. As an analog of charge in the electronic system, we define the "charge" [26,27] in the jth unit cell of the photonic system as

$$Q_j = \int_0^{\omega_{gap}} d\omega \int_j dr \rho(r, \omega). \tag{5}$$

Here the integration over the frequency is from 0 to a frequency in the band gap ω_{gap} that is below the eigenfrequencies of the edge and corner states. The physical meaning of the photonic "charge" represents the number of the photonic modes contributed from the jth unit cell below the band gap. Since our system considers the scatterers as perfect electrical

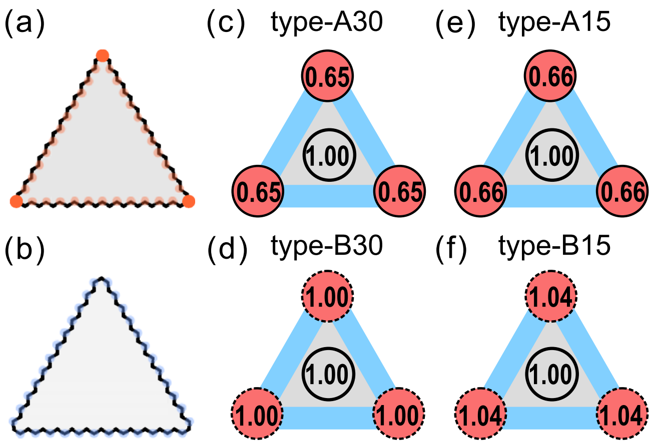

FIG. 5. Schematic of (a) type-A and (b) type-B structures where the outer layers of the structure are hidden for ease of visualization. The orange and blue dots indicate the Wannier center positions at the boundaries and corners. (c)–(f) Calculated "charge" per unit cell for bulk (gray) or corner (red) region in (c) type-A30, (d) type-B30, (e) type-A15, and (f) type-B15.

conductors, the magnetic field distributions are not concentrated in the hexagonal unit cell. To simplify the calculation, we redefine the unit cell as one of the red rhombuses in Figs. 3(a), 3(d), 4(a), and 4(e). The "charge" per unit cell in the bulk region is normalized to 1 because there is only one band below the band gap, and the "charge" for the corners can be obtained as shown in Figs. 5(c)–5(f). The corner charges are fractional and close to 2/3 in Figs. 5(c) and 5(e), which suggests the existence of topological corner states both in type-A30 and type-A15 structures. However, the calculated corner charges are integers (approximately equal to 1) in Figs. 5(d) and 5(f), which are consistent with the absence of topological corner states in type-B30 and type-B15 structures. According to the above discussions, there are three cases for a nested triangular structure by rotating the scatterers in a period of 120°, as illustrated in Fig. 6. Firstly, when $\theta \in (-60^\circ, 0^\circ)$, there is no topological corner states due to type-B configuration. Secondly, for $\theta \in (16^\circ, 44^\circ)$, topological corner states are localized in the band gap. Thirdly, for $\theta \in (7^\circ, 16^\circ)$ and $\theta \in (44^\circ, 53^\circ)$, they are embedded in bulk bands. The corner states embedded in bulk bands have been demonstrated in systems with C_4 and chiral symmetry, termed the higher-order

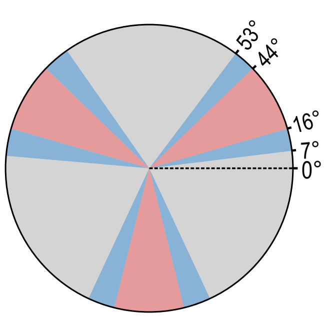

FIG. 6. Illustration of adjustable topological corner states. Red regions represent topological corner states localized within the band gap; blue regions represent topological corner states embedded in bulk bands; gray regions represent no topological corner state.

topological bound states in the continuum (BIC) [20,52–55]. In addition, embedded corner states in C_3 symmetric lattice were mentioned in sonic crystals in the Supplemental Materials of Ref. [33]. The conditions under which embedded corner states appear are elaborated in our system. They are sensitive to the width of the band gap. When there is not a wide enough band gap to isolate corner states, they will be embedded in bulk bands. Further reducing band-gap width will cause the hybridization of corner states and bulk states, making the corner states indistinguishable. For instance, in the cases of $\theta \in (0^\circ, 7^\circ)$ and $\theta \in (53^\circ, 60^\circ)$, topological corner states are absent, although they both fit the type-A configuration. Therefore, by continuously rotating the scatterers of our system, we can achieve adjustable topological corner states. This can be potentially applied to design THz topological functional devices.

IV. EXPERIMENTAL DEMONSTRATION OF TOPOLOGICAL CORNER STATES

In the experiments we fabricate different kinds of THz VPC samples. Steel wires with a diameter $d = 200\,\mu\text{m}$ are used as cylinders and arranged in the requirements of lattices. To make three steel wires tangent to each other in the unit cell, we etch a metal plate with particular chamfered triangular lattices [left panel of Fig. 7(a)], where the side length is 555 µm, and the lattice constant is 475 µm. The photograph of an assembled sample is shown in the right panel of Fig. 7(a), where we use two metal plates to maintain the lattice shape. Then we present the experiments of the bulk band gap in a VPC sample, the topological valley edge states in a waveguide channel consisting of two VPCs with opposite valley Chern numbers, and the topological corner states by constructing nested structures made of VPCs with two distinct higher-order topological phases.

The measurements are carried out using a THz real-time spectrometer (EKSPLA/THz, Lithuania), as schematically shown in Fig. 7(b). The linearly polarized THz waves along the y direction couple into the VPC sample from one end of the topological interface and have been collected by detectors. We obtain the transmittance spectrum by comparing the measured transmission spectrum intensity of the sample to the reference spectrum. Then the angle-resolved transmittance measurements are applied to identify the bulk band dispersions of the bulk sample. The sample comprises 40 unit cells along the x axis (length about 19.0 mm) and 4 unit cells along the y axis (width about 1.6 mm). The incident THz wave propagates along the y axis through the sample. Then we rotate the sample in the x-y plane along the z axis to change the incident angle α, causing the momentum component along the interface tangential component to vary continuously. Our experiments measure the transmittances when the incident angle α varies from 0° to 60°. These angle-resolved transmittances have been further merged into the dispersion map using the relation between the in-plane vector and incident angle α as $k_{//} = 2\pi \sin\alpha/\lambda$ (here λ is the wavelength of the incident THz wave). Figure 7(d) shows the measured dispersion map of VPC30$_+$, where the bulk band is branched, and the band gap is observed between 0.23 and 0.39 THz. This observation is consistent with the calculated photonic band structure

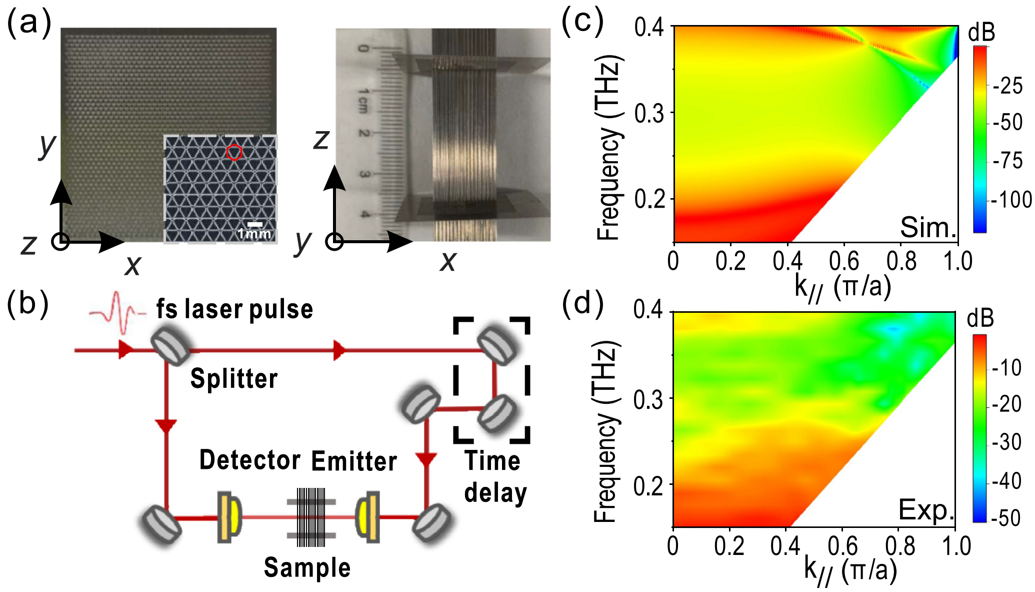

FIG. 7. (a) The left panel shows a photograph of a metal plate, where the inset is a magnification to show the detailed structure. An assembled experimental sample is shown in the right panel. (b) Experimental setup used to perform transmittance measurements. (c) Calculated and (d) Measured dispersion map for $VPC30_+$.

[as shown in Fig. 7(c)]. There is little difference between experimental data and numerically calculated results because of interface impedance matching and imprecise operations of the measurement process. Due to the geometric symmetry between $VPC30_+$ and $VPC30_-$, the $VPC30_-$ can be obtained by rotating 180° of $VPC30_+$ along the z axis. The dispersion map of $VPC30_-$ is the same as the result of $VPC30_+$. Therefore we have experimentally demonstrated the existence of a bulk band gap in $VPC30_+$ and $VPC30_-$.

Since the samples we fabricated are the VPCs, topological valley edge states should exist. To demonstrate the existence of topological edge states, we constructed a waveguide channel consisting of $VPC30_+$ and $VPC30_-$, and the former is placed on top of the latter, and they both comprised 10 unit cells along the x axis and 10-unit cells along the y axis as shown in Fig. 8(a). The simulated intensity distribution of $|H_z|$ in Fig. 8(b) indicates that the THz waves could propagate along the edge of the waveguide channel. In the experiment we measure the time-domain signal, $\boldsymbol{E}(t)$, of the sample with an edge waveguide channel and compare it to that of the bulk sample $VPC30_+$ shown in Fig. 8(c). After Fourier transforms, we can obtain the transmittances shown in Fig. 8(d). The results show that the transmittance is relatively low for bulk samples ranging from 0.23 to 0.39 THz. On the contrary, a sample with an interface waveguide channel exhibits relatively high transmittance at the same regime, suggesting the presence of topological valley edge states.

To experimentally verify the emergence of topological corner states, we fabricated several samples with type-A and type-B nested triangular structures, and two of them are shown in Fig. 9(a). In this experiment, to successfully excite and effectively detect the corner states is essential. We have designed and set up the optical path based on far-field detection as shown in Fig. 9(b). For THz waves with the frequency around the range of band gap, it is hard to spread across the x-y plane of the samples. Hence, THz waves can only radiate outward along the vertical plane direction, that is, along the metal antenna, and be detected. The simulations of electric field intensities $|E|^2$ are illustrated in Figs. 9(c)–9(f). When the frequency of incident THz waves is at 0.38 THz, only corner states can be easily excited for type-A30, but edge states are excited for type-B30 [as shown in Figs. 9(c) and 9(d)]. In the case of type-A15, except for corner states, bulk states are also excited, but the intensity of the former is greater [shown in Fig. 9(e)]. For type-B15, there is mainly a bulk state at 0.38 THz, as shown in Fig. 9(f). Meanwhile, in the experimental measurements, the distance between the sample and the detector along the z direction remains constant, while

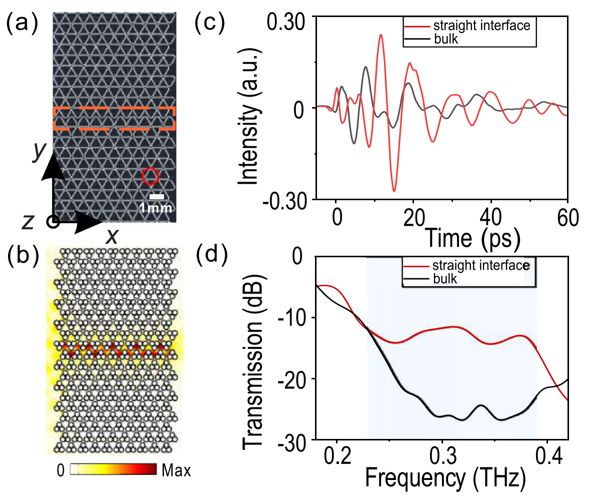

FIG. 8. (a) Photograph of a metal plate in which $VPC30_+$ is on the top and $VPC30_-$ is at the bottom. (b) The simulated field distribution of $|H_z|$ at 0.30 THz. (c) Measured time-domain spectra for the THz wave going through a straight interface (red curve) and the bulk (black curve). (d) Measured transmittance results for bulk (black curve) and edge states (red curve).

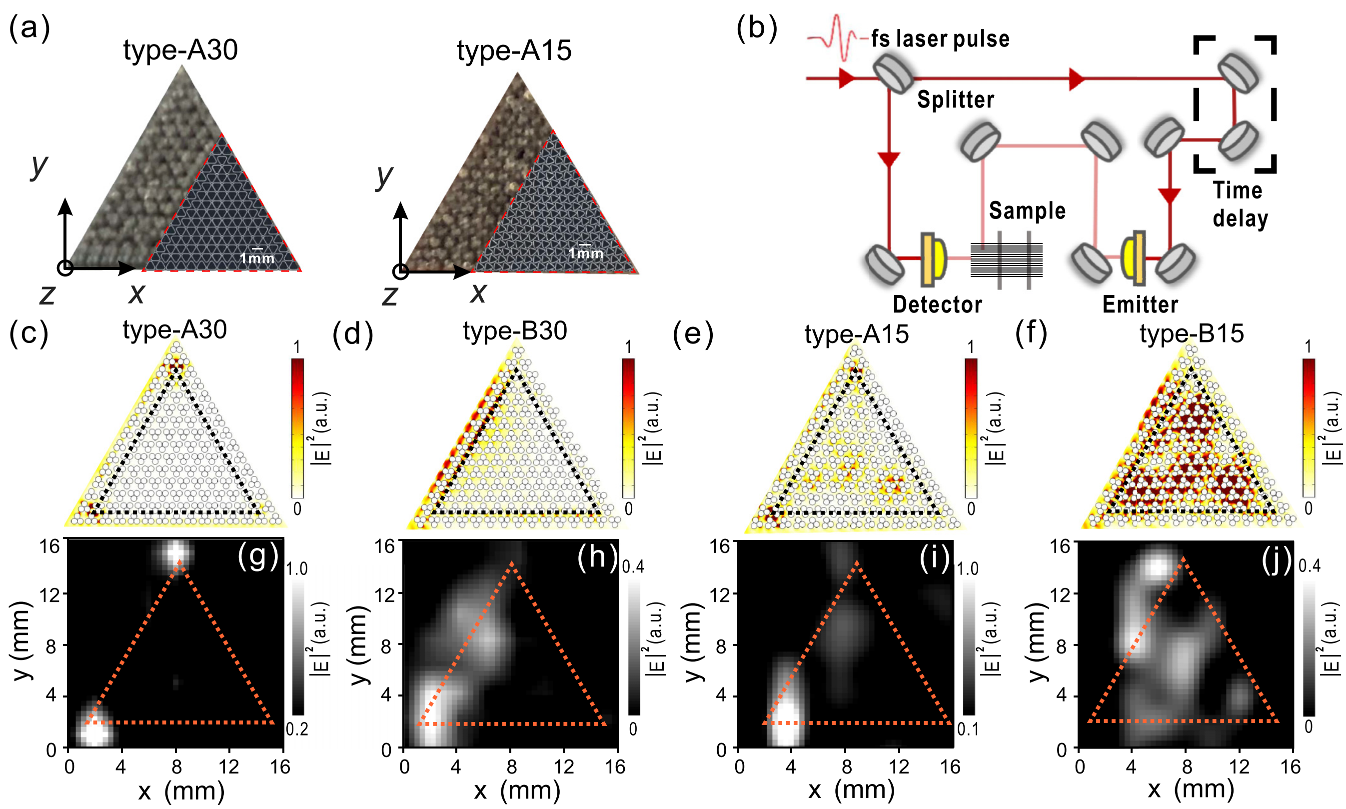

FIG. 9. (a) Photograph of fabricated samples in which type-A30 structure is shown on the left panel and type-A15 structure is on the right panel, where the inset is a magnification to show the detailed structure. (b) Experimental setup for measurements through the far-field radiation signal arriving at the detector. (c)–(f) Simulated electric field intensity $|E|^2$ under the excitation from the left for (c) type-A30, (d) type-B30, (e) type-A15, and (f) type-B15 structures at 0.38 THz, and black dashed lines represent the boundary in different nested triangular structures. (g)–(j) Measured spatial mapping of electric field intensity $|E|^2$ corresponding to (c)–(f), respectively, and orange dashed lines highlight the structures.

the relative position between the sample and the detector in the *x*-*y* plane is adjusted by moving the sample using a displacement platform. To enhance spatial resolution and minimize the impact of scattered THz waves, we have installed a narrow aperture with a diameter of 4 mm in front of the detector. Then the time-domain signals of different positions of the sample can be detected, and the spatial mapping of the electric field intensity of the sample is obtained by Fourier transform. For the type-A30 structure, we indeed observe the presence of corner states at a frequency of 0.38 THz, as shown in Fig. 9(g). Due to the fact that the far-field signals are collected in the experiments, the measured localized spots have a little bit of shift, but they clearly present the corner states, while the edge state is observed for the type-B30 structure at the same frequency [seen Fig. 9(h)]. When the rotation angle of scatterers of the system is 15°, the situation becomes different. It is shown in Fig. 9(i) that the corner states at the frequency of 0.38 THz remain localized around the corners. Meanwhile, the bulk states at the same frequency are excited inside the structure. In other words, the corner states are separated from the bulk states in space. Detachable topological corner states are generated, although they are embedded in bulk bands of eigenenergy spectra in type-A structures. However, it is different for the type-B15 structure, which only exhibits bulk states [illustrated in Fig. 9(j)]. Here, some electric fields exist outside the photonic crystals due to imperfections in the crystal samples, such as bending or unsmooth surfaces of steel wires. Additionally, it is worth noting that the spatial resolution of the electric field intensity measurements is approximately 3–4 mm, as illustrated in Figs. 9(g)–9(j). To enhance the resolution further, one could consider reducing the diameter of the circular aperture, but this may significantly impact the signal-to-noise ratio. However, two topological corner states are confirmed experimentally in type-A nested triangular structures [as shown in Figs. 9(g) and 9(i)].

V. SUMMARY

In conclusion, we have theoretically and experimentally investigated higher-order topological states in THz VPCs. With the triangular lattice, the broken mirror symmetry induced by rotating scatterers leads to the valley Hall effect and high-order topology. The valley topological phase transition of the structure is verified through calculated photonic band structure, phase profiles, and Berry curvature. Furthermore, topological corner states are demonstrated by numerical simulations of eigenenergy spectra, related field distributions, and LDOS of nested triangular structures. The results show that there are two types of topological corner states: one is within the band gap, and the other is embedded in the bulk. Both originate from bulk dipole moments protected by C_3

symmetry and can be switched flexibly by rotating the scatterers of the unit cells in the system. Then, by calculating the corner charge, it is found that the corresponding corner charge is fractional if corner states exist; the corner charge is an integer if there is no corner state. Experimentally, we fabricate a series of THz VPC samples. The angle-resolved transmittance measurements demonstrate the presence of the photonic band structure, and measured time-domain spectra reveal the valley edge states. Two topological corner states are directly observed by spatial mapping of the electric field intensity. These investigations provide the possibility of simultaneously employing topological corner, edge, and bulk states to guide THz waves, which may have potential applications in THz functional devices.

ACKNOWLEDGMENTS

This work was supported by the National Key R&D Program of China (Grants No. 2022YFA1404303 and No. 2020YFA0211300) and the National Natural Science Foundation of China (Grants No. 12234010, No. 61975078, and No. 11974177).

[1] L. Lu, J. D. Joannopoulos, and M. Soljačić, Topological photonics, Nat. Photon. **8**, 821 (2014).

[2] T. Ozawa, H. M. Price, A. Amo, N. Goldman, M. Hafezi, L. Lu, M. C. Rechtsman, D. Schuster, J. Simon, O. Zilberberg, and I. Carusotto, Topological photonics, Rev. Mod. Phys. **91**, 015006 (2019).

[3] G. Ma, M. Xiao, and C. T. Chan, Topological phases in acoustic and mechanical systems, Nat. Rev. Phys. **1**, 281 (2019).

[4] H. Xue, Y. Yang, and B. Zhang, Topological acoustics, Nat. Rev. Mater. **7**, 974 (2022).

[5] M.-J. Tuo, L.-H. Zhang, D. Liu, R.-W. Peng, R.-H. Fan, Z.-G. Chen, Y. Wu, D.-X. Qi, and M. Wang, Twist-projected two-dimensional acoustic topological insulators, Phys. Rev. B **99**, 205432 (2019).

[6] S. D. Huber, Topological mechanics, Nat. Phys. **12**, 621 (2016).

[7] H. Huang, J. Chen, and S. Huo, Recent advances in topological elastic metamaterials, J. Phys.: Condens. Matter **33**, 503002 (2021).

[8] W. A. Benalcazar, B. A. Bernevig, and T. L. Hughes, Quantized electric multipole insulators, Science **357**, 61 (2017).

[9] W. A. Benalcazar, B. A. Bernevig, and T. L. Hughes, Electric multipole moments, topological multipole moment pumping, and chiral hinge states in crystalline insulators, Phys. Rev. B **96**, 245115 (2017).

[10] W. A. Benalcazar, T. Li, and T. L. Hughes, Quantization of fractional corner charge in C_n-symmetric higher-order topological crystalline insulators, Phys. Rev. B **99**, 245151 (2019).

[11] B. Xie, H.-X. Wang, X. Zhang, P. Zhan, J.-H. Jiang, M. Lu, and Y. Chen, Higher-order band topology, Nat. Rev. Phys. **3**, 520 (2021).

[12] M. Serra-Garcia, V. Peri, R. Süsstrunk, O. R. Bilal, T. Larsen, L. G. Villanueva, and S. D. Huber, Observation of a phononic quadrupole topological insulator, Nature (London) **555**, 342 (2018).

[13] C. W. Peterson, W. A. Benalcazar, T. L. Hughes, and G. Bahl, A quantized microwave quadrupole insulator with topologically protected corner states, Nature (London) **555**, 346 (2018).

[14] S. Imhof, C. Berger, F. Bayer, J. Brehm, L. W. Molenkamp, T. Kiessling, F. Schindler, C. H. Lee, M. Greiter, T. Neupert, and R. Thomale, Topolectrical-circuit realization of topological corner modes, Nat. Phys. **14**, 925 (2018).

[15] S. Mittal, V. V. Orre, G. Zhu, M. A. Gorlach, A. Poddubny, and M. Hafezi, Photonic quadrupole topological phases, Nat. Photon. **13**, 692 (2019).

[16] X. Zhang, Z. K. Lin, H. X. Wang, Z. Xiong, Y. Tian, M. H. Lu, Y. F. Chen, and J. H. Jiang, Symmetry-protected hierarchy of anomalous multipole topological band gaps in nonsymmorphic metacrystals, Nat. Commun. **11**, 65 (2020).

[17] B.-Y. Xie, H.-F. Wang, H.-X. Wang, X.-Y. Zhu, J.-H. Jiang, M.-H. Lu, and Y.-F. Chen, Second-order photonic topological insulator with corner states, Phys. Rev. B **98**, 205147 (2018).

[18] X. D. Chen, W. M. Deng, F. L. Shi, F. L. Zhao, M. Chen, and J. W. Dong, Direct observation of corner states in second-order topological photonic crystal slabs, Phys. Rev. Lett. **122**, 233902 (2019).

[19] B. Y. Xie, G. X. Su, H. F. Wang, H. Su, X. P. Shen, P. Zhan, M. H. Lu, Z. L. Wang, and Y. F. Chen, Visualization of higher-order topological insulating phases in two-dimensional dielectric photonic crystals, Phys. Rev. Lett. **122**, 233903 (2019).

[20] Z.-G. Chen, C. Xu, R. Al Jahdali, J. Mei, and Y. Wu, Corner states in a second-order acoustic topological insulator as bound states in the continuum, Phys. Rev. B **100**, 075120 (2019).

[21] M. Li, D. Zhirihin, M. Gorlach, X. Ni, D. Filonov, A. Slobozhanyuk, A. Alù, and A. B. Khanikaev, Higher-order topological states in photonic kagome crystals with long-range interactions, Nat. Photon. **14**, 89 (2020).

[22] X.-T. He, M.-Y. Li, H.-Y. Qiu, W.-S. Ruan, L.-D. Zhou, L. Liu, X.-D. Chen, W.-J. Chen, F.-L. Zhao, and J.-W. Dong, In-plane excitation of a topological nanophotonic corner state at telecom wavelengths in a cross-coupled cavity, Photon. Res. **9**, 1423 (2021).

[23] H. Xue, Y. Yang, F. Gao, Y. Chong, and B. Zhang, Acoustic higher-order topological insulator on a kagome lattice, Nat. Mater. **18**, 108 (2019).

[24] X. Ni, M. Weiner, A. Alù, and A. B. Khanikaev, Observation of higher-order topological acoustic states protected by generalized chiral symmetry, Nat. Mater. **18**, 113 (2019).

[25] J. Noh, W. A. Benalcazar, S. Huang, M. J. Collins, K. P. Chen, T. L. Hughes, and M. C. Rechtsman, Topological protection of photonic mid-gap defect modes, Nat. Photon. **12**, 408 (2018).

[26] Y. Liu, S. Leung, F. F. Li, Z. K. Lin, X. Tao, Y. Poo, and J. H. Jiang, Bulk-disclination correspondence in topological crystalline insulators, Nature (London) **589**, 381 (2021).

[27] C. W. Peterson, T. Li, W. A. Benalcazar, T. L. Hughes, and G. Bahl, A fractional corner anomaly reveals higher-order topology, Science **368**, 1114 (2020).

[28] H.-X. Wang, L. Liang, B. Jiang, J. Hu, X. Lu, and J.-H. Jiang, Higher-order topological phases in tunable C_3 symmetric photonic crystals, Photon. Res. **9**, 1854 (2021).

[29] Y. Ota, F. Liu, R. Katsumi, K. Watanabe, K. Wakabayashi, Y. Arakawa, and S. Iwamoto, Photonic crystal nanocavity based on a topological corner state, Optica **6**, 786 (2019).
[30] R. Gong, M. Zhang, H. Li, and Z. Lan, Topological photonic crystal fibers based on second-order corner modes, Opt. Lett. **46**, 3849 (2021).
[31] H. R. Kim, M. S. Hwang, D. Smirnova, K. Y. Jeong, Y. Kivshar, and H. G. Park, Multipolar lasing modes from topological corner states, Nat. Commun. **11**, 5758 (2020).
[32] W. Zhang, X. Xie, H. Hao, J. Dang, S. Xiao, S. Shi, H. Ni, Z. Niu, C. Wang, K. Jin, X. Zhang, and X. Xu, Low-threshold topological nanolasers based on the second-order corner state, Light Sci. Appl. **9**, 109 (2020).
[33] X. Zhang, L. Liu, M. H. Lu, and Y. F. Chen, Valley-selective topological corner states in sonic crystals, Phys. Rev. Lett. **126**, 156401 (2021).
[34] S. An, T. Liu, H. Fan, H. Gao, Z. Gu, S. Liang, S. Huang, Y. Zheng, Y. Chen, L. Cheng, and J. Zhu, Second-order elastic topological insulator with valley-selective corner states, Int. J. Mech. Sci. **224**, 107337 (2022).
[35] Y. Dong, Y. Wang, J. Shi, S. Zhai, C. Ding, and X. Zhao, Multiband acoustic topological metamaterials with valley-switchable higher-order corner states, J. Phys. D: Appl. Phys. **55**, 435301 (2022).
[36] R. Zhou, H. Lin, Y. Wu, Z. Li, Z. Yu, Y. Liu, and D.-H. Xu, Higher-order valley vortices enabled by synchronized rotation in a photonic crystal, Photon. Res. **10**, 1244 (2022).
[37] Y. Zhang, T.-T. Tang, C. Girit, Z. Hao, M. C. Martin, A. Zettl, M. F. Crommie, Y. R. Shen, and F. Wang, Direct observation of a widely tunable bandgap in bilayer graphene, Nature (London) **459**, 820 (2009).
[38] K. F. Mak, K. L. McGill, J. Park, and P. L. McEuen, The valley Hall effect in MoS_2 transistors, Science **344**, 1489 (2014).
[39] T. Ma and G. Shvets, All-Si valley-Hall photonic topological insulator, New J. Phys. **18**, 025012 (2016).
[40] J.-W. Liu, F.-L. Shi, X.-T. He, G.-J. Tang, W.-J. Chen, X.-D. Chen, and J.-W. Dong, Valley photonic crystals, Adv. Phys. X **6**, 1905546 (2021).
[41] Y. L. Hong, G. H. Tang, R. W. Peng, R. H. Fan, Z. L. Ma, Z. Wang, Y. Jiang, L. D. Chen, and M. Wang, Direct observation of terahertz topological valley transport, Opt. Express **30**, 14839 (2022).
[42] J. Noh, S. Huang, K. P. Chen, and M. C. Rechtsman, Observation of photonic topological valley Hall edge states, Phys. Rev. Lett. **120**, 063902 (2018).
[43] R. H. Fan, Y. Zhou, X. P. Ren, R. W. Peng, S. C. Jiang, D. H. Xu, X. Xiong, X. R. Huang, and M. Wang, Freely tunable broadband polarization rotator for terahertz waves, Adv. Mater. **27**, 1201 (2015).
[44] R. H. Fan, B. Xiong, R. W. Peng, and M. Wang, Constructing metastructures with broadband electromagnetic functionality, Adv. Mater. **32**, 1904646 (2020).
[45] B. Ferguson and X.-C. Zhang, Materials for terahertz science and technology, Nat. Mater. **1**, 26 (2002).
[46] Y. Yang, Y. Yamagami, X. Yu, P. Pitchappa, J. Webber, B. Zhang, M. Fujita, T. Nagatsuma, and R. Singh, Terahertz topological photonics for on-chip communication, Nat. Photon. **14**, 446 (2020).
[47] A. Kumar, M. Gupta, P. Pitchappa, N. Wang, P. Szriftgiser, G. Ducournau, and R. Singh, Phototunable chip-scale topological photonics: 160 Gbps waveguide and demultiplexer for THz 6G communication, Nat. Commun. **13**, 5404 (2022).
[48] Y. Zeng, U. Chattopadhyay, B. Zhu, B. Qiang, J. Li, Y. Jin, L. Li, A. G. Davies, E. H. Linfield, B. Zhang, Y. Chong, and Q. J. Wang, Electrically pumped topological laser with valley edge modes, Nature (London) **578**, 246 (2020).
[49] J. Wang, Y. Liu, D. Yang, Z. Hu, X. Zhang, S. Xia, D. Song, M. Ren, S. Gao, R. Wang, Z. Chen, and J. Xu, Tunable terahertz topological edge and corner states in designer surface plasmon crystals, Opt. Express **29**, 19531 (2021).
[50] Y. Zhao, F. Liang, J. Han, X. Wang, D. Zhao, and B. Z. Wang, Tunable topological edge and corner states in an all-dielectric photonic crystal, Opt. Express **30**, 40515 (2022).
[51] H.-X. Wang, G.-Y. Guo, and J.-H. Jiang, Band topology in classical waves: Wilson-loop approach to topological numbers and fragile topology, New J. Phys. **21**, 093029 (2019).
[52] W. A. Benalcazar and A. Cerjan, Bound states in the continuum of higher-order topological insulators, Phys. Rev. B **101**, 161116(R) (2020).
[53] A. Cerjan, M. Jürgensen, W. A. Benalcazar, S. Mukherjee, and M. C. Rechtsman, Observation of a higher-order topological bound state in the continuum, Phys. Rev. Lett. **125**, 213901 (2020).
[54] Z. Hu, D. Bongiovanni, D. Jukić, E. Jajtić, S. Xia, D. Song, J. Xu, R. Morandotti, H. Buljan, and Z. Chen, Nonlinear control of photonic higher-order topological bound states in the continuum, Light Sci. Appl. **10**, 164 (2021).
[55] Y. Wang, B. Y. Xie, Y. H. Lu, Y. J. Chang, H. F. Wang, J. Gao, Z. Q. Jiao, Z. Feng, X. Y. Xu, F. Mei, S. Jia, M. H. Lu, and X. M. Jin, Quantum superposition demonstrated higher-order topological bound states in the continuum, Light Sci. Appl. **10**, 173 (2021).